

Reversible regulation of thermal conductivity through spin-crossover transitions

Qichen Song¹, Rahil Ukani¹, Vidhya M. Dev¹, Hong Ki Kim¹, Jungwoo Shin², Jinyoung Seo¹, Caleb Stamper^{3,4}, Ryan D. McGillicuddy¹, Jason J. Calvin¹, Yukyung Moon¹, Catherine Thai¹, Jason D. Braun¹, Dehong Yu⁴, Gang Chen², Jarad A. Mason^{1*}

¹Department of Chemistry and Chemical Biology, Harvard University, Cambridge, MA 02138, USA

²Department of Mechanical Engineering, Massachusetts Institute of Technology, Cambridge, MA 02139, USA

³Institute for Superconducting and Electronic Materials, University of Wollongong, Wollongong, NSW 2500, Australia

⁴Australian Nuclear Science and Technology Organisation, Lucas Heights, NSW 2234, Australia

Abstract

The development of strategies to modulate the thermal conductivity of a solid in response to an external stimulus is critical to the creation of high-performance thermal regulators, thermal switches, and thermal diodes—devices which would be enabling for a wide range of emerging technologies. Here, we report a new mechanism for achieving switchable solid-state thermal conductivity through a first-order spin-crossover phase transition. Specifically, we show that the molecular spin-crossover complex $\text{Fe}[\text{HB}(\text{tz})_3]_2$ [$\text{HB}(\text{tz})_3^- = \text{hydrotris}(1,2,4\text{-triazol-1-yl})\text{borate}$] exhibits a large drop in thermal conductivity—more than four-fold—across its electronic spin transition. This thermal conductivity change is highly reversible and can be attributed to lower group velocities of heat-carrying phonons and increased phonon scattering in the high-spin phase of the compound as a result of weaker metal–ligand bonds. Owing to the large structural and chemical diversity of spin-crossover materials and the rich variety of stimuli that can induce electronic spin transitions, these results establish a powerful approach to manipulating thermal transport within solid materials.

*mason@chemistry.harvard.edu

31 **Main**

32 Phase transitions often lead to large changes in the internal properties of a material in response to
33 a small change in the external environment. A high contrast in the properties that can be reversibly
34 accessed when switching between two phases is an enabling feature of phase-change materials for
35 many applications. Though changes to free energy, density, and electronic, magnetic, optical, and
36 mechanical properties have been well studied across a diverse range of solid-state phase transitions,
37 much remains to be understood about how phase transitions impact thermal conductivity¹. This
38 represents an important knowledge gap since the ability to modulate thermal transport within a
39 solid material is critical to realizing next-generation thermal devices—such as thermal switches^{2,3},
40 thermal diodes⁴, and thermal regulators⁵—that would provide new opportunities for more efficient
41 and higher performance heat management⁶, solid-state cooling⁷, and thermal energy storage^{8,9}
42 technologies.

43 Several types of phase transitions—including martensitic transitions¹⁰, amorphous-crystalline
44 transitions¹¹, rotational transitions^{12,13}, conformational transitions¹⁴, and metal-insulator
45 transitions^{15,16}—have been shown to be accompanied by changes in thermal conductivity, but the
46 library of materials for which thermal conductivity changes have been measured across a phase
47 transition is modest in scope and lacking in structural and chemical diversity. Moreover, challenges
48 associated with low switching ratios, poor reversibility, large hysteresis, slow response times,
49 inconsistent experimental data, and large volume changes that can lead to functional fatigue have
50 made it difficult to implement phase-change materials in functional thermal devices^{17–19}. This is
51 particularly true for thermally induced phase transitions, which are important for passive thermal
52 regulation²⁰.

53 In pursuit of a phase-change mechanism capable of inducing large thermal conductivity changes
54 without large changes to the internal structure and composition of a material—in order to promote
55 reversibility and fast kinetics—we were drawn to electronic spin-crossover transitions. Spin-
56 crossover (SCO) transitions occur when the ground-state electronic configuration of a molecule or
57 material—most commonly composed of Fe(II) centers bound to N-donor organic ligands—
58 switches between a low-spin (LS) and high-spin (HS) state. This switching arises when the free
59 energy difference between the two states is small because of a balance between the energy
60 difference between valence d orbitals—as dictated by the ligand field—and the energy required to
61 pair two electrons in the same orbital. In such a case, enthalpic effects drive the system to a LS
62 configuration at low temperatures, and entropic effects drive a transition to a HS configuration at
63 higher temperatures.

64 The entropic driving force for a SCO transition arises both from an increase in electronic entropy
65 due to the presence of more unpaired electrons in the HS state [13.4 J mol⁻¹ K⁻¹ for d⁶ Fe(II)] and
66 from an increase in phonon (vibrational) entropy as electrons populate metal–ligand molecular
67 orbitals that have greater anti-bonding character. The latter effect is also responsible for the
68 weakening of metal–ligand bonds that accompanies most SCO transitions. We hypothesized that

69 this bond weakening could have a large effect on thermal transport within a SCO material by
70 softening the crystal lattice and altering the phonon density of states. Indeed, the spin state of Fe
71 centers has been shown to impact the thermal conductivity of the Earth's lower mantle²¹ and certain
72 molecular Fe(III) complexes²². To the best of our knowledge, however, there have not been any
73 reports of thermal conductivity changes across a discrete first-order SCO phase transition in a
74 material.

75 In order to begin investigating the impact of a first-order SCO transition on thermal conductivity,
76 we sought a SCO material with 1) a sharp transition between a single low-spin and single high-
77 spin state, 2) minimal thermal hysteresis, 3) no spectator charge-balancing ions, and 4) a compact
78 ligand scaffold. Though there are many compounds that could satisfy these criteria, we selected
79 the Fe(II)-based molecular coordination complex $\text{Fe}[\text{HB}(\text{tz})_3]_2$ [$\text{HB}(\text{tz})_3^-$ = hydrotris(1,2,4-triazol-
80 1-yl)borate] as a particularly well-suited initial candidate for switchable thermal conductivity
81 across a SCO transition²³. This neutral, mononuclear complex consists of an Fe(II) center bound
82 to two tridentate, anionic organic ligands in a trigonal antiprismatic coordination geometry (D_{3d}
83 symmetry). In the solid state, $\text{Fe}[\text{HB}(\text{tz})_3]_2$ crystallizes into an orthorhombic lattice²⁴ held together
84 through a combination of weak hydrogen bonding and van der Waals interactions between
85 complexes (Fig. 1a). As has been previously reported²⁵, the compound undergoes a highly
86 cooperative SCO transition at 332 K between a singlet ($S = 0$) state at low temperatures and a
87 quintet ($S = 2$) state at high temperatures (Figs. 1b, 1c, and 1e). This transition is accompanied by
88 an overall volume expansion of 3.6% that arises from an average increase in Fe–N bond lengths
89 of 0.16 Å (8%), but the SCO transition does not lead to any changes to the lattice structure of the
90 material or the relative orientation of individual complexes. Notably, this SCO transition is highly
91 reversible with a thermal hysteresis of less than 1 K and negligible changes to the phase-change
92 properties even after ten million thermal cycles²⁶.

93 To assess the impact of the SCO transition on thermal transport, we used frequency-domain
94 thermoreflectance (FDTR) to measure the thermal conductivity of individual single crystals of
95 $\text{Fe}[\text{HB}(\text{tz})_3]_2$ as a function of temperature. Specifically, a continuous-wave (CW) pump laser ($\lambda =$
96 458 nm) was modulated at a certain frequency and used to heat the sample periodically (Fig. 1f)^{27,28}.
97 A thin-film (93 nm) gold transducer layer was deposited on $\text{Fe}[\text{HB}(\text{tz})_3]_2$ crystals in order to
98 convert the energy of the photons from the pump laser into heat. The temperature oscillations at
99 the surface of the metal transducer were then measured through the thermoreflectance of a probe
100 laser beam ($\lambda = 532$ nm). The temperature modulations at the surface have a phase lag with respect
101 to the phase of the pump heating power that is related to the thermal conductivity of the underlying
102 sample, along with the sample heat capacity and the thermal boundary conductance between the
103 transducer and sample. Compared to traditional techniques for measuring the thermal conductivity
104 of macroscopic samples, FDTR offers the advantage of providing a direct probe of the intrinsic
105 thermal conductivity within a material, without complications from interparticle heat transfer
106 inherent in the pellet sample geometry²⁹.

107 It is immediately clear from the raw FDTR data that the phase lag for $\text{Fe}[\text{HB}(\text{tz})_3]_2$ abruptly
108 increases after the SCO transition from the LS to HS phase over a modulation frequency range of
109 0.8 MHz to 30 MHz (Fig. 1g), which suggests a sudden drop in thermal conductivity. By fitting
110 the FDTR data with a Fourier heat conduction model and independently measuring the temperature
111 dependence of the heat capacity of $\text{Fe}[\text{HB}(\text{tz})_3]_2$ (Fig. 1d) (see Supplementary Information for
112 details), the thermal conductivity of $\text{Fe}[\text{HB}(\text{tz})_3]_2$ was extracted and found to exhibit a large drop
113 across the SCO transition, from $0.70 \text{ W m}^{-1} \text{ K}^{-1}$ (323 K) in the LS phase to $0.16 \text{ W m}^{-1} \text{ K}^{-1}$ (340 K)
114 in the HS phase (Fig. 1h). To further validate these results, we performed FDTR measurements on
115 several different $\text{Fe}[\text{HB}(\text{tz})_3]_2$ single crystals and a $\text{Fe}[\text{HB}(\text{tz})_3]_2$ crystal coated with a $\text{Au}_{0.93}\text{Ti}_{0.07}$
116 alloy transducer layer instead of a pure Au layer, observing similar thermal conductivity changes
117 in all cases (Fig. S6). To evaluate the reversibility of this thermal conductivity switching, we heated
118 and cooled an individual $\text{Fe}[\text{HB}(\text{tz})_3]_2$ single crystal through the SCO transition 30 times (Fig. 2a).
119 The phase lags and thermal conductivities of the LS and HS phases were very consistent during
120 each cycle, as was the thermal conductivity switching behavior.

121 The change in thermal conductivity that $\text{Fe}[\text{HB}(\text{tz})_3]_2$ experiences as a result of the SCO transition
122 is remarkable, particularly considering that it occurs over such a narrow temperature range ($< 20 \text{ K}$)
123 and involves such a small structural change ($< 0.2 \text{ \AA}$ increase in Fe–N bond lengths). Indeed, the
124 thermal conductivity switching ratio for $\text{Fe}[\text{HB}(\text{tz})_3]_2$ exceeds those reported for other thermal
125 phase-change materials (Fig. 2b), including ones that undergo solid-liquid melting transitions
126 ($\text{Ge}_2\text{Sb}_2\text{Te}_5$, Hg, H_2O , $\text{CaCl}_2 \cdot 6\text{H}_2\text{O}$, $\text{Ba}(\text{OH})_2 \cdot 8\text{H}_2\text{O}$, $\text{MgCl}_2 \cdot 6\text{H}_2\text{O}$ and paraffin wax)^{30–32},
127 structural transitions (Ni–Mn–In¹⁰, C_{60} ¹², and $[\text{Co}_6\text{Se}_8][\text{C}_{60}]$ ¹³), and metal-insulator transitions (a
128 VO_2 thin film¹⁵ and nanowire¹⁶). While crystalline polyethylene nanofibers can exhibit a high
129 switching ratio, they are excluded from our comparison due to the proximity of the structural phase
130 transition to the melting temperature, which compromises the reversibility and operating range of
131 the materials.

132 We sought to gain additional insight into the microscopic origins of the large thermal conductivity
133 contrast in $\text{Fe}[\text{HB}(\text{tz})_3]_2$ through a combination of inelastic neutron scattering experiments, Raman
134 scattering experiments, and quantum mechanical simulations. With a low electrical conductivity
135 ($< 10^{-6} \text{ S/m}$)³⁴, heat within $\text{Fe}[\text{HB}(\text{tz})_3]_2$ will be primarily conducted through lattice vibrations
136 (phonons)—the properties of which will be impacted by the SCO transition and can be directly
137 probed by inelastic neutron scattering³⁵. Specifically, the generalized phonon density of states is
138 given by $\text{GDOS}(\omega) = \int g(Q, \omega) dQ$, where $g(Q, \omega)$ is the normalized inelastic neutron scattering
139 function, given by $g(Q, \omega) = \frac{\omega}{(n(\omega, T) + 1)Q^2} S(Q, \omega)$. Here, $n(\omega, T)$ is the Bose-Einstein distribution
140 function, and $S(Q, \omega)$ is the dynamic neutron scattering function of the sample at the momentum
141 transfer $\hbar Q$ and phonon frequency ω , which is normalized to ensure $\int \text{GDOS}(\omega) = 3N/V$, where
142 N is the number of atoms in the unit cell and V is the volume of the unit cell. As depicted in Figs.
143 3a and 3b, we observe clear changes to the normalized inelastic neutron scattering function during
144 the SCO transition. Notably, two shallow gaps between the phonon bands centered at 2.7 THz, 4.3

145 THz, and 5.9 THz disappear in the HS phase as these bands all shifts to lower energies. The
146 disappearance of these shallow gaps should allow for more three-phonon scattering processes to
147 occur by making it easier to satisfy energy conservation, which would contribute to decreasing
148 thermal conductivity. By evaluating the three-phonon scattering phase space (Eq. S25), we
149 estimate a decrease in phonon lifetime by a factor of at least 1.5 across the SCO transition for
150 phonons below 4 THz (Fig. 3g).

151 The GDOS for Fe[HB(tz)₃]₂ shows that phonon bands below 12 THz experience a substantial
152 softening (decrease in frequency) during the transition from the LS to HS phase (Fig. 3c). For
153 example, the optical phonon peak at 5.9 THz shifts to 4.8 THz, and the optical phonon peak at 4.3
154 THz shifts to 3.0 THz. On average, the frequencies of optical phonon peaks between 4 THz and 8
155 THz decrease by a factor of $\left(\frac{\omega_{\text{LS}}}{\omega_{\text{HS}}}\right)^2 = 1.6$ during the SCO transition (Fig. 3d), which directly leads
156 to a reduction in the off-diagonal element of the group velocity matrix, v_{ij} , that is responsible for
157 heat transfer via wave-like phonon tunneling^{36,37} by a factor of $\left(\frac{v_{\text{LS},ij}}{v_{\text{HS},ij}}\right)^2 \approx \left(\frac{\omega_{\text{LS}}}{\omega_{\text{HS}}}\right)^2$ (Fig. S7). In
158 addition, the GDOS shows minimal variation with temperature within each spin state, highlighting
159 that the changes in phonon properties can be attributed to the SCO transition rather than to a
160 temperature effect. The prominent peak in the vibrational spectra measured by Stokes Raman
161 scattering aligns well with that in the GDOS obtained from inelastic neutron scattering (Fig. 3f).
162 Importantly, the suppression of the high-frequency modes and promotion of the low-frequency
163 modes provide additional support for optical phonon softening across the SCO transition.

164 The group velocity, v , of the acoustic phonons, which can be extracted by fitting the low-energy
165 GDOS according to the scaling relation $\text{GDOS}(\omega) \approx \frac{3\omega^2}{2\pi^2 v^3}$, decreases substantially from the LS
166 phase at 300 K to the HS phase at 350 K with $\left(\frac{v_{\text{LS}}}{v_{\text{HS}}}\right)^2 = 1.5$ (Fig. 3e). This decreased phonon
167 velocity will suppress the thermal conductivity due to particle-like phonon transport by the same
168 factor. The reduction in group velocity is also in good agreement with that observed in the Fe
169 partial vibrational density of states determined by resonant nuclear inelastic scattering³⁸. Moreover,
170 nanoindentation measurements suggest a group velocity decrease from 2432 m/s at 318 K to 1755
171 m/s at 343 K with $\left(\frac{v_{\text{LS}}}{v_{\text{HS}}}\right)^2 = 1.9$ (Fig. S22). Though both inelastic neutron scattering and
172 nanoindentation experiments show that the SCO transition has the same effect on group velocity,
173 differences in the magnitude of the decrease determined by each technique may be the result of
174 the anisotropic nature of the SCO transition in Fe[HB(tz)₃]₂, for which the structural expansion
175 occurs preferentially along the crystallographic *c* axis. Regardless, the observed redshifts of
176 phonon frequencies and reduction in acoustic phonon velocities directly contribute to the reduction
177 in thermal conductivity of Fe[HB(tz)₃]₂ after the SCO transition.

178 To better understand the origins of phonon softening at a molecular level, we studied the lattice
179 dynamics in Fe[HB(tz)₃]₂ using quantum mechanical simulations. Since it is challenging to directly

compute the interatomic force constants at the density-functional-theory (DFT) level—as there are 188 atoms in the primitive unit cell—we used the density functional tight-binding (DFTB) method. The relaxed atomic structures of both the LS and HS phases calculated using DFTB are in good agreement with the experimental single crystal structures (Fig. S24). As Fe–N bond lengths increase during the SCO transition, the force constants $\Psi_{ij}^{\alpha=\beta}$ for Fe atom i and N atom j moving along the same Cartesian axis decrease by a factor of 2 to 4 (Fig. 4a). These weaker bonds favor softer phonons, as the magnitudes of the force constants, $|\Psi_{ij}^{\alpha\beta}|$, scale with the phonon frequency squared, ω^2 . Hydrogen bonding interactions between molecular complexes also show a modest decrease in their absolute force constants as the average hydrogen bond length slightly elongates (by <1%) during the SCO transition (Fig. 4b). Since intramolecular and intermolecular bonding collectively determine the lattice dynamics, the square of the ratio between phonon frequencies at the Γ point (the center of the 1st Brillouin zone) in the LS and HS phases $[(\omega_{\text{LS}}/\omega_{\text{HS}})^2]$ decreases as the phonon frequency of the LS phase (ω_{LS}) increases (Fig. 4c), and the highest value is above 1.9. This is consistent with the phonon softening observed by inelastic neutron scattering, nanoindentation and Raman scattering. Moreover, the phonon polarization vectors experience subtle changes from the LS to HS phase (Fig. 4e), as reflected in the increased amplitudes of hydrogen-bond librations—angular bond oscillations that are intrinsically softer than bond-stretching vibrations (Fig. S27).

To evaluate the relative contributions of intramolecular and intermolecular interactions to lattice vibrations, we defined a mode-resolved metric, $\eta_\lambda = \frac{\mathbf{u}_\lambda^\dagger \mathbf{D}_{\text{inter}} \mathbf{u}_\lambda}{\mathbf{u}_\lambda^\dagger (\mathbf{D}_{\text{inter}} + \mathbf{D}_{\text{intra}}) \mathbf{u}_\lambda}$, as the ratio between the vibrational energy associated with intermolecular interactions and the total vibrational energy in the unit cell. Here, $\mathbf{D}_{\text{inter}}$ and $\mathbf{D}_{\text{intra}}$ are dynamical matrices constructed at the Γ point using the calculated intermolecular and intramolecular force constants, respectively, and \mathbf{u}_λ is the eigenvector of phonon mode λ (see Supplementary Information for more detail). In both spin states, phonons possess less intermolecular character with increasing frequency (Fig. 4d). This suggests that more intramolecular bonds are involved in higher frequency phonons, increasing the relative importance of $\mathbf{D}_{\text{intra}}$ compared to $\mathbf{D}_{\text{inter}}$. At lower frequencies, optical phonon modes with $\eta_\lambda > 80\%$ are present in HS state but not the LS states, which is another manifestation of phonon softening because of weakened intramolecular interactions ($\mathbf{D}_{\text{intra}}$). Overall, our calculations reveal that changes in bond strengths and in specific vibrational features—particularly the contribution of librational modes—rather than structural and symmetry variations, are responsible for the softening of the entire lattice.

The foregoing results demonstrate that electronic spin-state transitions in coordination complexes can lead to large, reversible changes in the thermal conductivity of a solid material over a narrow temperature range. Unlike most approaches to thermal conductivity switching that rely primarily on tuning the phonon scattering lifetime (anharmonicity) through large structural changes, the SCO transition directly modulates the phonon group velocity through small changes to metal–ligand

217 bond lengths. The small volume change that accompanies these changes should simplify the
218 fabrication of thermal devices. Moreover, there are myriad possibilities for manipulating SCO
219 materials through ligand design, including the ability to synthesize compounds that are connected
220 by 1-, 2-, or 3-D networks of coordination bonds. In addition to temperature, SCO transitions can
221 also be induced by hydrostatic pressure³⁹ and, in some cases, light⁴⁰, a voltage bias⁴¹, an applied
222 magnetic field⁴², or uptake of guest molecules⁴³. This tunability and sensitivity to a range of
223 external stimuli provides a vast design space for leveraging SCO transitions to manipulate thermal
224 transport.

References

1. Chen, H. *et al.* Thermal conductivity during phase transitions. *Adv. Mater.* **31**, 1806518 (2019).
2. Lu, Q. *et al.* Bi-directional tuning of thermal transport in SrCoO_x with electrochemically induced phase transitions. *Nat. Mater.* **19**, 655–662 (2020).
3. Li, M. *et al.* Electrically gated molecular thermal switch. *Science* **382**, 585–589 (2023).
4. Chang, C. W., Okawa, D., Majumdar, A. & Zettl, A. Solid-state thermal rectifier. *Science* **314**, 1121–1124 (2006).
5. Zheng, R., Gao, J., Wang, J. & Chen, G. Reversible temperature regulation of electrical and thermal conductivity using liquid–solid phase transitions. *Nat. Commun.* **2**, 1–6 (2011).
6. Browne, M. C., Norton, B. & McCormack, S. J. Phase change materials for photovoltaic thermal management. *Renew. Sustain. Energy Rev.* **47**, 762–782 (2015).
7. Klinar, K. & Kitanovski, A. Thermal control elements for caloric energy conversion. *Renew. Sustain. Energy Rev.* **118**, 109571 (2020).
8. Gur, I., Sawyer, K. & Prasher, R. Searching for a better thermal battery. *Science* **335**, 1454–1455 (2012).
9. Usman, A., Xiong, F., Aftab, W., Qin, M. & Zou, R. Emerging solid-to-solid phase-change materials for thermal-energy harvesting, storage, and utilization. *Adv. Mater.* **34**, 2202457 (2022).
10. Zheng, Q., Zhu, G., Diao, Z., Banerjee, D. & Cahill, D. G. High contrast thermal conductivity change in Ni–Mn–In Heusler alloys near room temperature. *Adv. Eng. Mater.* **21**, 1801342 (2019).
11. Lyeo, H. K. *et al.* Thermal conductivity of phase-change material Ge₂Sb₂Te₅. *Appl. Phys. Lett.* **89**, 151904 (2006).
12. Yu, R. C., Tea, N., Salamon, M. B., Lorents, D. & Malhotra, R. Thermal conductivity of single crystal C₆₀. *Phys. Rev. Lett.* **68**, 2050–2053 (1992).
13. Ong, W. L. *et al.* Orientational order controls crystalline and amorphous thermal transport in superatomic crystals. *Nat. Mater.* **16**, 83–88 (2016).
14. Shin, J. *et al.* Light-triggered thermal conductivity switching in azobenzene polymers. *Proc. Natl. Acad. Sci. U. S. A.* **116**, 5973–5978 (2019).
15. Oh, D. W., Ko, C., Ramanathan, S. & Cahill, D. G. Thermal conductivity and dynamic heat capacity across the metal-insulator transition in thin film VO₂. *Appl. Phys. Lett.* **96**, 151906 (2010).
16. Lee, S. *et al.* Anomalously low electronic thermal conductivity in metallic vanadium dioxide. *Science* **355**, 371–374 (2021).

17. Yuan, K. *et al.* Engineering the thermal conductivity of functional phase-change materials for heat energy conversion, storage, and utilization. *Adv. Funct. Mater.* **30**, 1904228 (2020).
18. Li, Y. *et al.* Transforming heat transfer with thermal metamaterials and devices. *Nat. Rev. Mater.* **6**, 488–507 (2021).
19. Swoboda, T., Klinar, K., Yalamarthy, A. S., Kitanovski, A. & Muñoz Rojo, M. Solid-state thermal control devices. *Adv. Electron. Mater.* **7**, 2000625 (2021).
20. Wehmeyer, G., Yabuki, T., Monachon, C., Wu, J. & Dames, C. Thermal diodes, regulators, and switches: Physical mechanisms and potential applications. *Appl. Phys. Rev.* **4**, 41304 (2017).
21. Hsieh, W. P., Deschamps, F., Okuchi, T. & Lin, J. F. Effects of iron on the lattice thermal conductivity of Earth’s deep mantle and implications for mantle dynamics. *Proc. Natl. Acad. Sci. U. S. A.* **115**, 4099–4104 (2018).
22. Hoshino, N., Hayashi, A. & Akutagawa, T. The strong correlations between thermal conductivities and electronic spin states in the crystals of Fe(III) spin crossover complexes. *Dalt. Trans.* **51**, 12698–12703 (2022).
23. Janiak, C. *et al.* Effects of nitrogen substitution in poly(pyrazolyl)borato ligands: from orbital energy levels to C–H···O hydrogen bonding. *Chem. – A Eur. J.* **2**, 992–1000 (1996).
24. Rat, S. *et al.* Solvatomorphism and structural-spin crossover property relationship in bis[hydrotris(1,2,4-triazol-1-yl)borate]iron(II). *CrystEngComm* **19**, 3271–3280 (2017).
25. van Koningsbruggen, P. J. & Miller, J. S. Observation of a 331 K (58 °C) spin transition for bis[hydrotris(1,2,4-triazol-1-yl)borate]iron(II) by variable temperature infrared spectroscopy and magnetic susceptibility measurements. *Solid State Sci.* **10**, 1804–1806 (2008).
26. Ridier, K. *et al.* Unprecedented switching endurance affords for high-resolution surface temperature mapping using a spin-crossover film. *Nat. Commun.* **11**, 1–9 (2020).
27. Schmidt, A. J., Cheaito, R. & Chiesa, M. A frequency-domain thermoreflectance method for the characterization of thermal properties. *Rev. Sci. Instrum.* **80**, 094901 (2009).
28. Yang, J., Ziade, E. & Schmidt, A. J. Modeling optical absorption for thermoreflectance measurements. *J. Appl. Phys.* **119**, 095107 (2016).
29. Olson, D. H., Braun, J. L. & Hopkins, P. E. Spatially resolved thermoreflectance techniques for thermal conductivity measurements from the nanoscale to the mesoscale. *J. Appl. Phys.* **126**, 150901 (2019).
30. Crespi, L., Ghetti, A., Boniardi, M. & Lacaita, A. L. Electrical conductivity discontinuity at melt in phase change memory. *IEEE Electron Device Lett.* **35**, 747–749 (2014).
31. Ho, C. Y., Powell, R. W. & Liley, P. E. Thermal conductivity of the elements. *J. Phys. Chem. Ref. Data* **1**, 279–421 (1972).

32. Lane, G. A. Low temperature heat storage with phase change materials. *Int. J. Ambient Energy* **1**, 155–168 (1980).
33. Shrestha, R. *et al.* High-contrast and reversible polymer thermal regulator by structural phase transition. *Sci. Adv.* **5**, 3777–3790 (2019).
34. Zhang, Y. *et al.* Switching endurance of the molecular spin crossover complex $[\text{Fe}(\text{HB}(\text{tz})_3)_2]$: from single crystals to thin films and electronic devices. *Mater. Adv.* **3**, 8193–8200 (2022).
35. Furrer, A., Mesot, J. & Strässle, T. Neutron scattering in condensed matter physics. *Neutron Scatt. Condens. Matter Phys.* 1–317 (2009).
36. Simoncelli, M., Marzari, N. & Mauri, F. Unified theory of thermal transport in crystals and glasses. *Nat. Phys.* **15**, 809–813 (2019).
37. Isaeva, L., Barbalinardo, G., Donadio, D. & Baroni, S. Modeling heat transport in crystals and glasses from a unified lattice-dynamical approach. *Nat. Commun.* **10**, 1–6 (2019).
38. Mikolasek, M. *et al.* Complete set of elastic moduli of a spin-crossover solid: spin-state dependence and mechanical actuation. *J. Am. Chem. Soc.* **140**, 8970–8979 (2018).
39. Seo, J., Braun, J. D., Dev, V. M. & Mason, J. A. Driving barocaloric effects in a molecular spin-crossover complex at low pressures. *J. Am. Chem. Soc.* **144**, 6493–6503 (2022).
40. Chastanet, G., Lorenc, M., Bertoni, R. & Desplanches, C. Light-induced spin crossover—Solution and solid-state processes. *Comptes Rendus Chim.* **21**, 1075–1094 (2018).
41. Osorio, E. A. *et al.* Electrical manipulation of spin states in a single electrostatically gated transition-metal complex. *Nano Lett.* **10**, 105–110 (2010).
42. Bousseksou, A. *et al.* Dynamic response of the spin-crossover solid $\text{Co}(\text{H}_2(\text{fsa})_2\text{en})(\text{py})_2$ to a pulsed magnetic field. *Phys. Rev. B* **65**, 172412 (2002).
43. Halder, G. J., Kepert, C. J., Moubaraki, B., Murray, K. S. & Cashion, J. D. Guest-dependent spin crossover in a nanoporous molecular framework material. *Science* **298**, 1762–1765 (2002).
44. Song, Q., Warkander, S. & Huberman, S. C. Probing carrier and phonon transport in semiconductors all at once through frequency-domain photoreflectance. *Phys. Rev. Appl.* **21**, 034044 (2024).
45. Yang, J., Ziade, E. & Schmidt, A. J. Uncertainty analysis of thermoreflectance measurements. *Rev. Sci. Instrum.* **87**, 14901 (2016).
46. Dehong, Y., Richard, M., Terry, N., Shane, K. & Robert, R. Pelican — a time of flight cold neutron polarization analysis spectrometer at OPAL. *J. Phys. Soc. Japan* **82**, SA027 (2013).
47. Grimme, S., Bannwarth, C. & Shushkov, P. A robust and accurate tight-binding quantum chemical method for structures, vibrational frequencies, and noncovalent interactions of large molecular systems parametrized for all spd-block elements ($Z = 1–86$). *J. Chem. Theory Comput.* **13**, 1989–2009 (2017).

48. Shi, Q., Boerio-Goates, J. & Woodfield, B. F. An improved technique for accurate heat capacity measurements on powdered samples using a commercial relaxation calorimeter. *J. Chem. Thermodyn.* **43**, 1263–1269 (2011).
49. Feser, J. P., Liu, J. & Cahill, D. G. Pump-probe measurements of the thermal conductivity tensor for materials lacking in-plane symmetry. *Rev. Sci. Instrum.* **85**, 104903 (2014).
50. Jiang, P., Qian, X. & Yang, R. A new elliptical-beam method based on time-domain thermoreflectance (TDTR) to measure the in-plane anisotropic thermal conductivity and its comparison with the beam-offset method. *Rev. Sci. Instrum.* **89**, 94902 (2018).
51. Tang, L. & Dames, C. Anisotropic thermal conductivity tensor measurements using beam-offset frequency domain thermoreflectance (BO-FDTR) for materials lacking in-plane symmetry. *Int. J. Heat Mass Transf.* **164**, 120600 (2021).
52. Cahill, D. G. Analysis of heat flow in layered structures for time-domain thermoreflectance. *Rev. Sci. Instrum.* **75**, 5119–5122 (2004).
53. Mathews, J. & Walker, R. L. *Mathematical Methods of Physics*. (W.A. Benjamin, 1970).
54. Carslaw, H. S. & Jaeger, J. C. *Conduction of Heat in Solids*. (Oxford University Press, 1959).
55. Ravichandran, N. K. & Broido, D. Phonon-phonon interactions in strongly bonded solids: selection rules and higher-order processes. *Phys. Rev. X* **10**, 021063 (2020).
56. Ashcroft, N. W. & Mermin, N. D. *Solid State Physics*. (Cengage Learning, 1976).
57. West, D. & Estreicher, S. K. First-principles calculations of vibrational lifetimes and decay channels: hydrogen-related modes in Si. *Phys. Rev. Lett.* **96**, 115504 (2006).
58. Shulumba, N., Hellman, O. & Minnich, A. J. Intrinsic localized mode and low thermal conductivity of PbSe. *Phys. Rev. B* **95**, 14302 (2017).
59. Parr, R. G. & Weitao, Y. *Density-functional theory of atoms and molecules*. (Oxford University Press, 1994).
60. Bochevarov, A. D. *et al.* Jaguar: A high-performance quantum chemistry software program with strengths in life and materials sciences. *Int. J. Quantum Chem.* **113**, 2110–2142 (2013).
61. Slater, J. C. & Phillips, J. C. *Quantum theory of molecules and solids*. (McGraw Hill, New York, 1974).
62. Vosko, S. H. *et al.* Accurate spin-dependent electron liquid correlation energies for local spin density calculations: a critical analysis. *CaJPh* **59**, 1200 (1980).
63. Becke, A. D. Density-functional exchange-energy approximation with correct asymptotic behavior. *Phys. Rev. A* **38**, 3098 (1988).
64. Lee, C., Yang, W. & Parr, R. G. Development of the Colle-Salvetti correlation-energy formula into a functional of the electron density. *Phys. Rev. B* **37**, 785 (1988).
65. Grimme, S., Antony, J., Ehrlich, S. & Krieg, H. A consistent and accurate ab initio

parametrization of density functional dispersion correction (DFT-D) for the 94 elements H—Pu. *J. Chem. Phys.* **132**, 154104 (2010).

66. Ditchfield, R., Hehre, W. J. & Pople, J. A. Self-consistent molecular-orbital methods. IX. An extended Gaussian-type basis for molecular-orbital studies of organic molecules. *J. Chem. Phys.* **54**, 724–728 (1971).
67. Hay, P. J. & Wadt, W. R. *Ab initio* effective core potentials for molecular calculations. Potentials for K to Au including the outermost core orbitals. *J. Chem. Phys.* **82**, 299–310 (1985).
68. Wadt, W. R. & Hay, P. J. *Ab initio* effective core potentials for molecular calculations. Potentials for main group elements Na to Bi. *J. Chem. Phys.* **82**, 284–298 (1985).
69. Hay, P. J. & Wadt, W. R. *Ab initio* effective core potentials for molecular calculations. Potentials for the transition metal atoms Sc to Hg. *J. Chem. Phys.* **82**, 270–283 (1985).
70. Dunning, T. H. Gaussian basis sets for use in correlated molecular calculations. I. The atoms boron through neon and hydrogen. *J. Chem. Phys.* **90**, 1007–1023 (1989).
71. Rashin, A. A. & Honig, B. Reevaluation of the Born model of ion hydration. *J. Phys. Chem.* **89**, 5588–5593 (1985).
72. Zimmermann, R. & König, E. A model for high-spin/low-spin transitions in solids including the effect of lattice vibrations. *J. Phys. Chem. Solids* **38**, 779–788 (1977).
73. Nishino, M., Boukheddaden, K., Konishi, Y. & Miyashita, S. Simple two-dimensional model for the elastic origin of cooperativity among spin states of spin-crossover complexes. *Phys. Rev. Lett.* **98**, 247203 (2007).
74. Rafizadeh, H. A. & Yip, S. Lattice dynamics of hexamine—a rigid-molecule approximation. *J. Chem. Phys.* **53**, 315–325 (1970).
75. Boča, R. Zero-field splitting in metal complexes. *Coord. Chem. Rev.* **248**, 757–815 (2004).

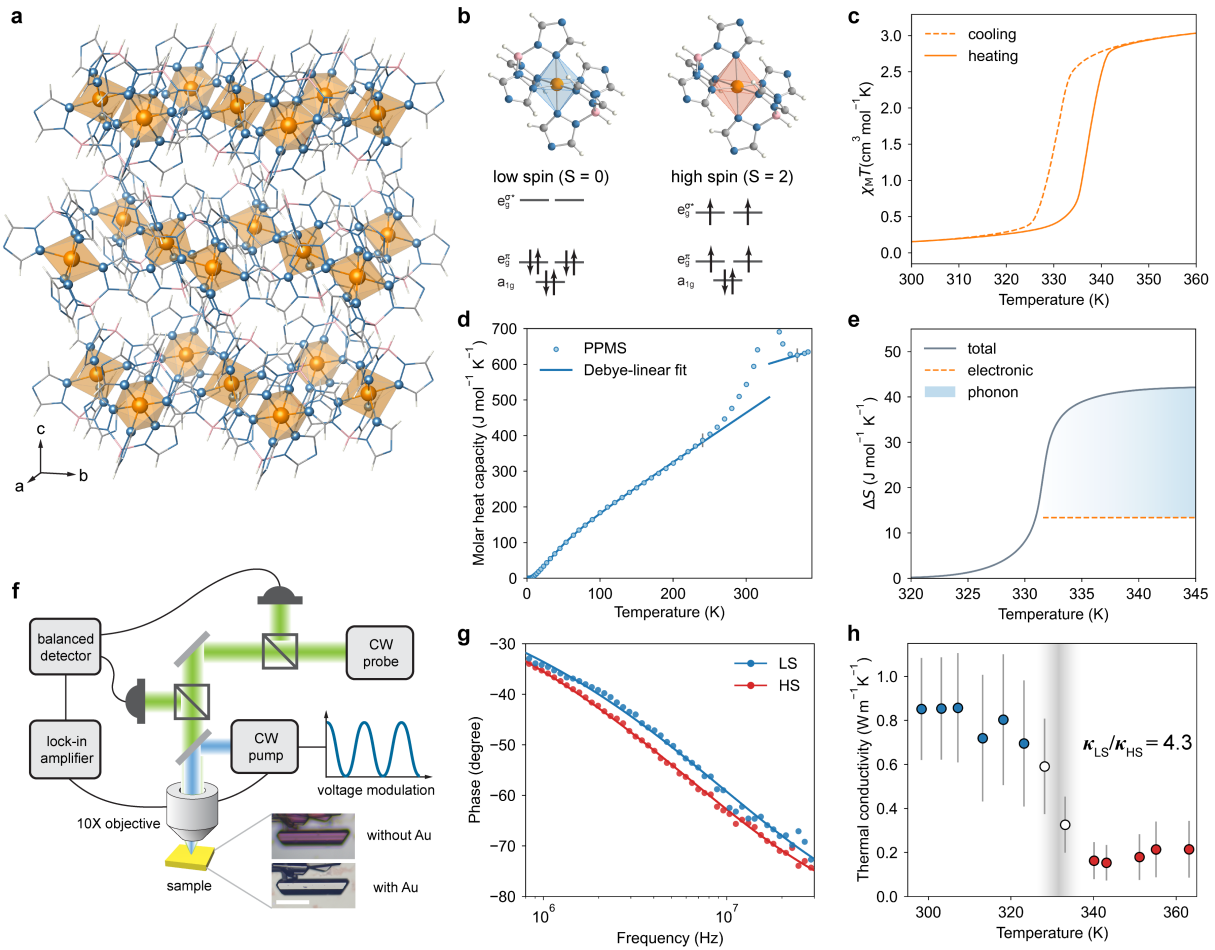


Fig. 1 | Thermal conductivity changes across a spin-crossover phase transition. **a**, Crystal structure of $\text{Fe}[\text{HB}(\text{tz})_3]_2$ in the LS phase to illustrate the weak, non-covalent interactions between molecular complexes in the solid state. Orange and blue spheres represent Fe and N atoms, respectively. Grey, blue, white, and pink rods represent C, N, H, and B atoms, respectively. **b**, The atomic structure and valence electronic structure of the LS and HS phases of $\text{Fe}[\text{HB}(\text{tz})_3]_2$. Grey, blue, white, pink, and orange spheres represent C, N, H, B, and Fe atoms, respectively. **c**, Temperature dependence of the product of magnetic susceptibility and temperature ($\chi_M T$) for $\text{Fe}[\text{HB}(\text{tz})_3]_2$, highlighting the low hysteresis associated with its spin-crossover transition. **d**, Experimental heat capacity of $\text{Fe}[\text{HB}(\text{tz})_3]_2$ as measured by a PPMS (blue circles) and a fit (blue line) that combines a Debye model with a linear function of temperature. Temperatures near the phase transition—as indicated by the region marked with vertical lines—are excluded from the model fitting. **e**, The phonon (vibrational) entropy change (shaded region) represents ~71% of the total entropy change (gray line) associated with the SCO transition of $\text{Fe}[\text{HB}(\text{tz})_3]_2$, with the balance being due to a change in electronic entropy (orange dashed line). **f**, A schematic of the frequency-domain thermoreflectance (FDTR) instrument used to measure the thermal conductivity of single crystals of $\text{Fe}[\text{HB}(\text{tz})_3]_2$ as a function of temperature. The insets show optical microscope images of a $\text{Fe}[\text{HB}(\text{tz})_3]_2$ single crystal in the LS phase with and without the gold transducer layer. Scale bar, 100 μm . **g**, The phase lag of the thermoreflectance signal from FDTR measurements (dots) and best fits from a Fourier heat conduction model (lines) are shown for the LS (318 K) and HS (343 K) phase of $\text{Fe}[\text{HB}(\text{tz})_3]_2$. **h**, The temperature dependence of thermal conductivity for $\text{Fe}[\text{HB}(\text{tz})_3]_2$ determined from FDTR measurements for a single crystal of $\text{Fe}[\text{HB}(\text{tz})_3]_2$ in the LS (blue circles) and HS (red circles) phase. The shaded region represents a temperature window of 10 K centered around $T_{\text{tr}} = 331$ K where the two spin phases can coexist. Error bars represent the uncertainty in the best fit, evaluated using Monte Carlo simulations.

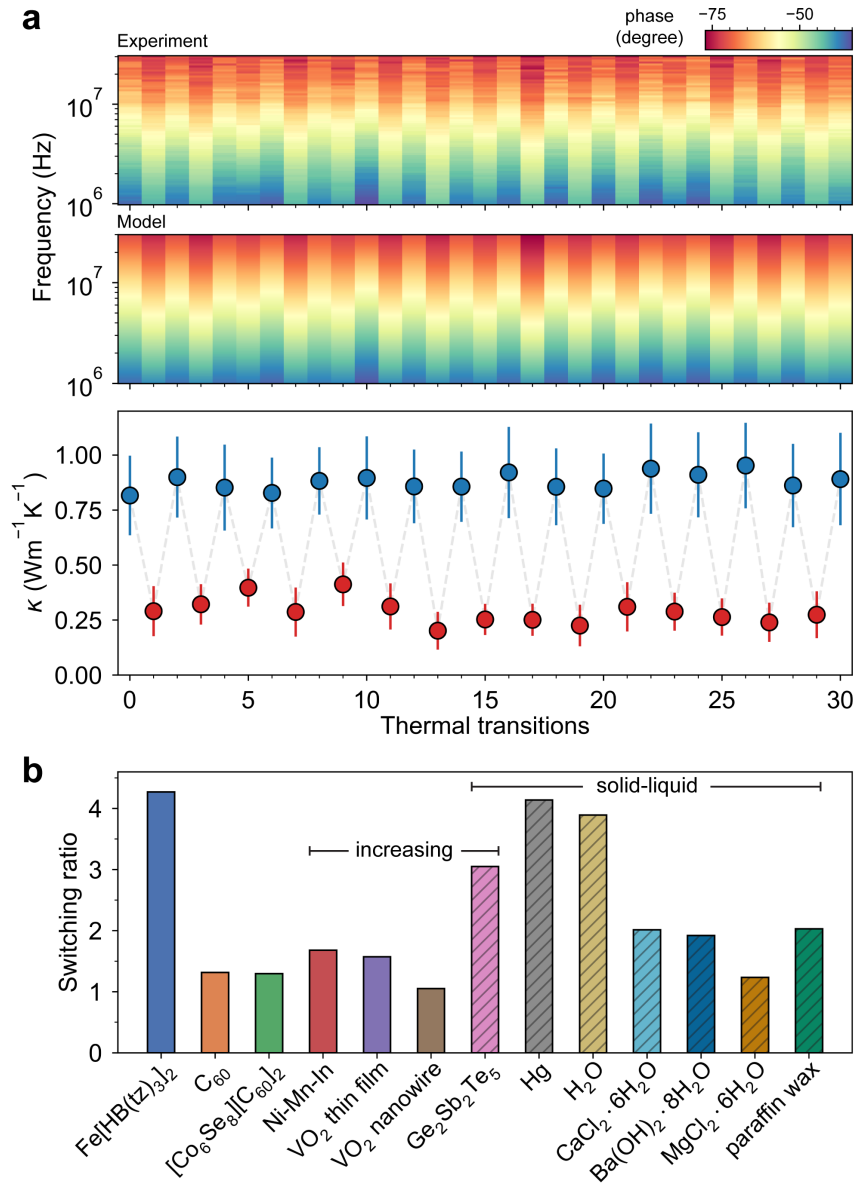


Fig. 2 | Reversible thermal conductivity switching in Fe[HB(tz)₃]₂. **a**, The phase lag of the thermorelectance signal from FDTR measurements (top) and best fits from a Fourier heat conduction model (middle) are represented by colormaps for 30 thermal transitions between 303 K and 343 K. The thermal conductivity determined at 303 K (blue) and 343 K (red) within each cycle (bottom). **b**, The thermal conductivity switching ratios of representative solid-solid and solid-liquid phase-change materials are compared. All materials exhibit decreased thermal conductivity in their high-temperature phases, with the exception of the 4 materials indicated as "increasing".

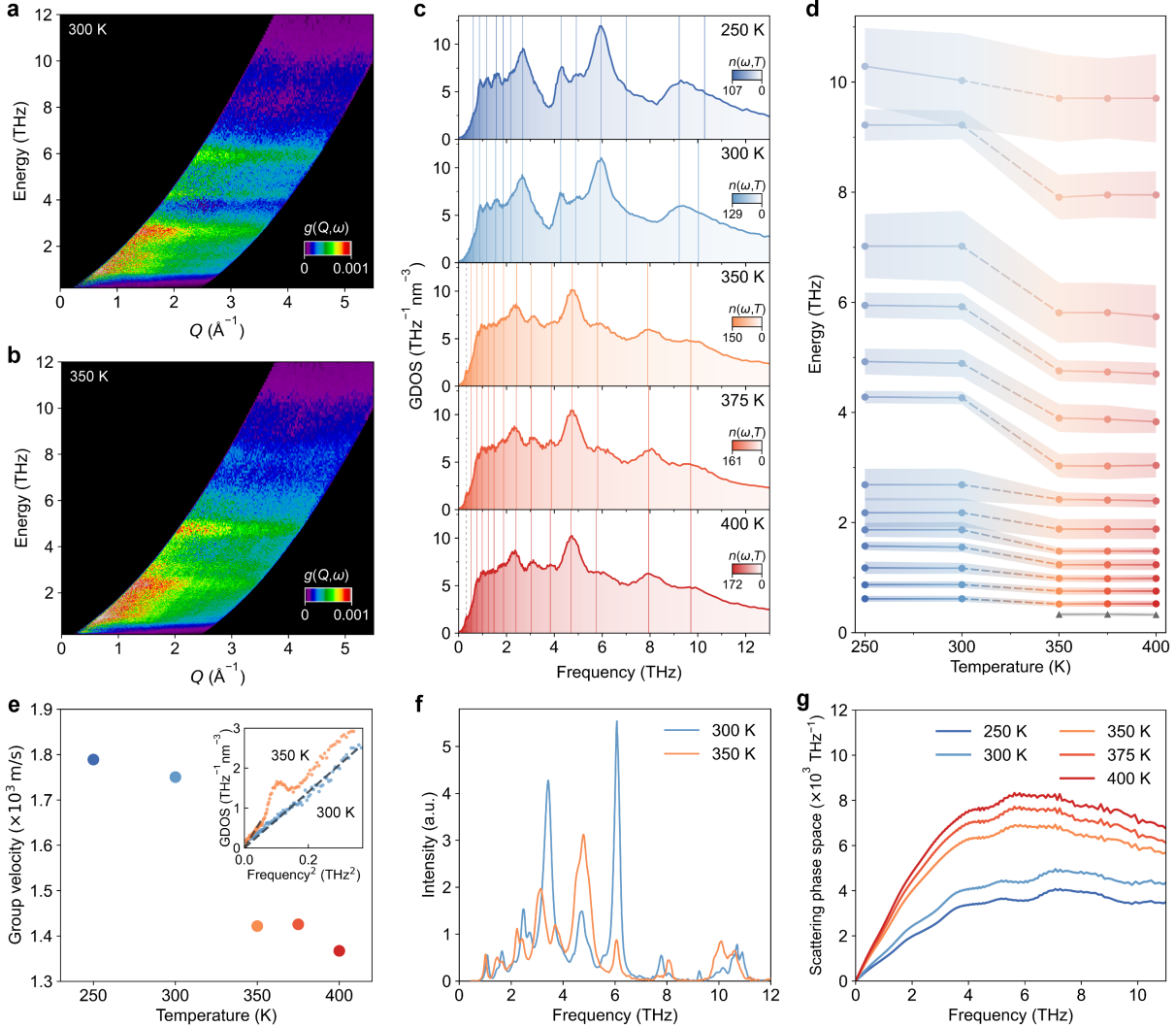


Fig. 3 | Phonon softening observed in inelastic neutron scattering and Raman scattering. **a,b**, The normalized inelastic neutron scattering function $g(Q,\omega)$ at a given momentum transfer and energy for the LS (**a**) and HS (**b**) phases of $\text{Fe}[\text{HB}(\text{tz})_3]_2$. **c**, The generalized phonon density of states, $\text{GDOS}(\omega)$, for the LS phase at 250 K and 300 K and for the HS phase at 350 K, 375 K and 400 K. The solid lines correspond to optical phonon peaks from pseudo-Voigt fits, while the dashed lines in HS phases represent zero-field splitting-related excitations. The color gradient represents the Bose-Einstein distribution function $n(\omega,T)$ (the phonon occupation number), ranging from 0 to $n(0.2 \text{ meV},T)$, with darker colors indicating higher occupation numbers. **d**, The peak positions of all optical phonon bands from pseudo-Voigt fits as a function of temperature. The shaded area represents the full width at half-maximum of each peak. Note that the narrow, lowest-energy peak emerging in the HS phase (dark gray) is due to the presence of unpaired electrons. **e**, Temperature-dependent phonon group velocity. The inset illustrates that the low-frequency GDOS scales with ω^2 and the scaling factor (inversely related to phonon group velocity) changes significantly when the spin state changes. **f**, Ultra-low-frequency Stokes Raman scattering intensity for the LS and HS phases. The Raman scattering intensity is normalized by the factor $\frac{n(\omega,T)+1}{\omega}$. **g**, The three-phonon scattering phase space—a measure of the number of possible energy-conserving phonon scattering events—as a function of frequency at different temperatures.

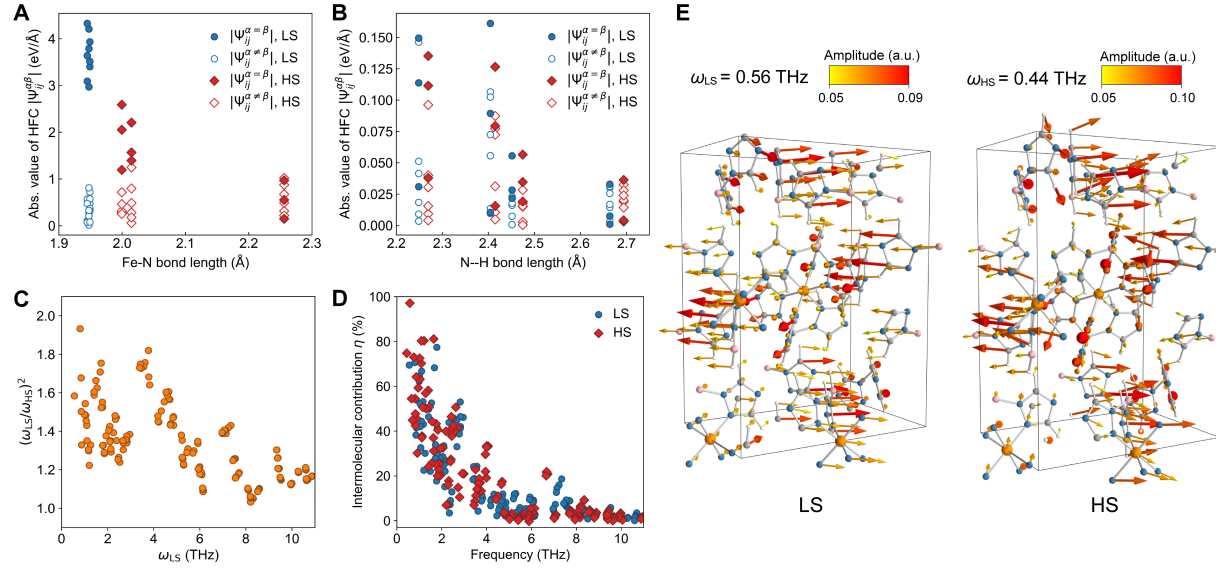


Fig. 4 | Contributions of intra- and intermolecular interactions to thermal transport. **a,b,** The intramolecular harmonic force constants of Fe–N bonds (**a**) and the intermolecular harmonic force constants of N–H hydrogen bonds (**b**). The filled and unfilled markers correspond to the harmonic force constants where atom i and atom j move along the same ($\alpha = \beta$) and different ($\alpha \neq \beta$) Cartesian axes, respectively. **c,** The ratio of the optical phonon frequencies in the LS and HS phases. **d,** The contribution of intermolecular vibrations to phonons in the LS and HS phases. **e,** The phonon polarization vectors in the unit cell of $\text{Fe}[\text{HB}(\text{tz})_3]_2$ for the lowest-energy optical phonon mode with $\omega_{LS} = 0.56$ THz in the LS phase and $\omega_{HS} = 0.44$ THz in the HS phase. The color and length of the arrows reflect the amplitude of the polarization vector.

Acknowledgements

We thank Catherine Badding for assistance with the heat capacity measurements and Svetlana Boriskina for helpful discussions. Neutron beam time was awarded at the Australian Nuclear Science and Technology Organisation under proposal P17369. This work was performed in part at the Harvard University Center for Nanoscale Systems (CNS), a member of the National Nanotechnology Coordinated Infrastructure Network (NNCI), which is supported by the National Science Foundation under NSF award number ECCS-2025158. Q.S. acknowledges the support from the Harvard Quantum Initiative.

Author contributions

J.A.M. and J.Se. developed the initial idea for this research, and J.A.M. supervised the project. Q.S. and J.Sh. conducted the FDTR measurements and performed the analysis. V.M.D. and J.D.B. grew the single crystals and conducted the SQUID measurements. Q.S., R.U., C.T. and R.D.M. contributed to sample preparation. Q.S. performed the phonon calculations and theoretical analysis and G.C. contributed to this analysis. H.K.K. performed the DFTB and DFT calculations. R.U., C.S. and D.Y. conducted the neutron scattering experiments. Q.S., R.U. and V.M.D. conducted the Raman scattering measurements. R.U. conducted the nanoindentation measurement. R.D.M. and R.U. performed DSC measurements. J.J.C., R.U., and R.D.M. conducted heat capacity measurements. Q.S., Y.M. and R.U. developed the alloy transducer. Q.S., J.Se., and J.A.M. wrote the manuscript. All authors contributed to data analysis and editing the manuscript.

Competing interests

J.A.M, J.Se., R.D.M., J.D.B. and R.U. are inventors on a patent application related to this work held and submitted by Harvard University.